ACSNANO www.acsnano.org

ARTICLE

Spatially Resolved Chemical Detection with a Nanoneedle-Probe-Supported Biological Nanopore

Kan Shoji,[†,‡] Ryuji Kawano,[†] and Ryan J. White*[,‡,§]

[†]Department of Biotechnology and Life Science, Tokyo University of Agriculture and Technology, 2-24-16 Naka-cho, Koganei-shi, Tokyo 184-8588, Japan

[‡]Department of Chemistry and [§]Department of Electrical Engineering and Computer Science, University of Cincinnati, Cincinnati, Ohio 45221-0172, United States

Supporting Information

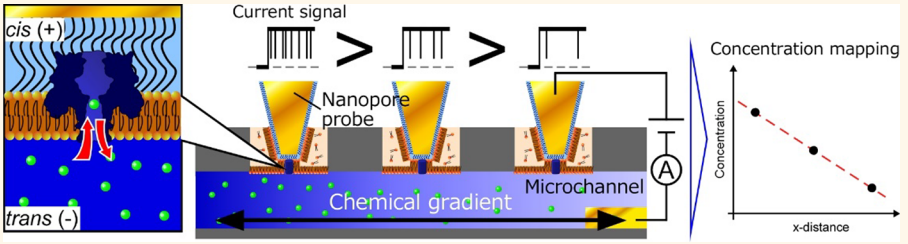

ABSTRACT: In this article, we describe the quantitative characterization of a gold nanoneedle ion channel probe and demonstrate the utility of this probe for spatially resolved detection of a small molecule using ion channel activity. Our report builds on recent reports of Ide and co-workers, who reported the use of an etched gold wire modified with a poly(ethylene) glycol monolayer as a support for a lipid bilayer and subsequent single ion channel recordings. Although this nanoneedle electrode approach was reported previously, in our report, we investigate the effects of several operational parameters on the performance of the ion channel measurement and electrochemical phenomenon that occur in the nanoconfined space between the supported bilayer and the gold electrode. More specifically, we address the effects of length of the supporting monolayer and the composition of the electrolyte baths on channel current measurements and provide a quantitative description of what carries current at the working electrode (double-layer charging). In addition, we demonstrate the ability to control the direction of protein insertion (tip side *vs* bath side) with freely diffusing protein, which has not been previously reported, with the former method (tip side) enabling single-molecule detection of β-cyclodextrin (βCD) using a reconstituted α-hemolysin channel. Finally, anticipating future use of a nanoneedle-based biological nanopore probe in a scanned-probe microscopy, we demonstrate the ability to quantify and spatially resolve the concentration of βCD molecules in a microfluidic channel. We believe, in the long term, the described nanoneedle-based biological nanopore probe can be employed in, for example, scanning ion conductance microscopy using ion channels.

KEYWORDS: *nanopore, resistive pulse, α-hemolysin, imaging, nanoneedle, lipid bilayer membrane*

Resistive-pulse nanopore sensors that measure blockage currents caused by single molecules binding to, or translocating through, a nanopore provide single-molecule sensing with high sensitivity, temporal resolution, signal-to-noise ratio, and molecular selectivity.[1−6] These sensors have been applied as DNA sequencers[7−9] and sensors for biomolecules including miRNAs[5,10−13] and proteins.[14−17] Solid-state nanopores[18,19] typically fabricated by exposing thin membranes such as silicon nitride and carbon to a high-energy electron beam or biological nanopores,[20] which comprise pore-forming proteins reconstituted into a lipid bilayer membrane, are key examples of the types of nanopores utilized in this sensing strategy. Although both show promise for sensing applications, biological nanopores (*i.e.*, protein channels) provide reproducible pore sizes dictated by the protein structure and have thus found widespread use as resistive-pulse detectors.

To employ biological nanopores for sensing purposes, a stable lipid bilayer membrane is required. Whereas the painting method[21] and the Montal−Mueller method[22] are generally used, resulting in the formation of a membrane spanning across a pore in a hydrophobic substrate, these methods are time-consuming and the resulting membrane is unstable to

Received: December 21, 2018
Accepted: February 6, 2019
Published: February 6, 2019

DOI: 10.1021/acsnano.8b09667
ACS Nano XXXX, XXX, XXX−XXX

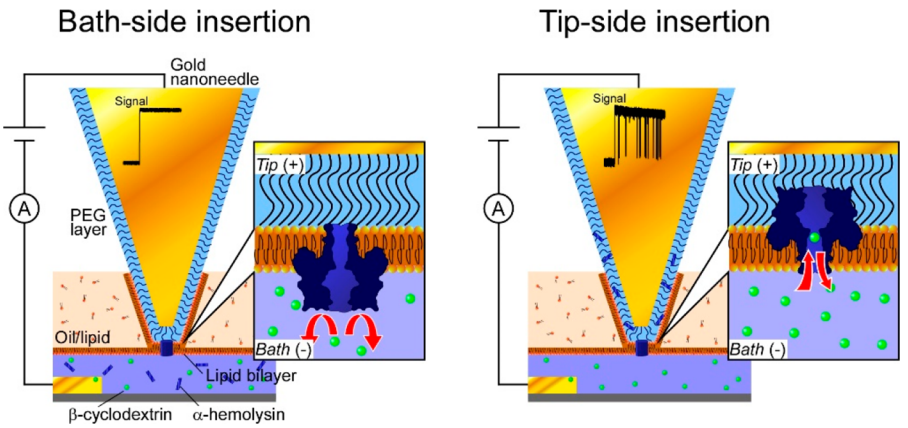

Figure 1. Schematic illustrations of the nanoneedle-based nanopore probe. Probes are composed of an electrochemically etched gold microwire that is modified with a thiolated PEG layer. The probe is immersed across an oil/lipid aqueous interface to form a bilayer at the electrode surface. (Left) Bath-side protein insertion is achieved by incorporating protein in the aqueous bath layer. In this configuration, *β*CD in the bath solution do not interact with *α*HL. (Right) Conversely, with tip-side insertion, *α*HL inserts from the aqueous solution reservoir between the bilayer and gold surface. In this configuration, bath-side *β*CD molecules enter the *trans* side of the *α*HL pores, resulting in single-molecule binding events in the current−time trace.

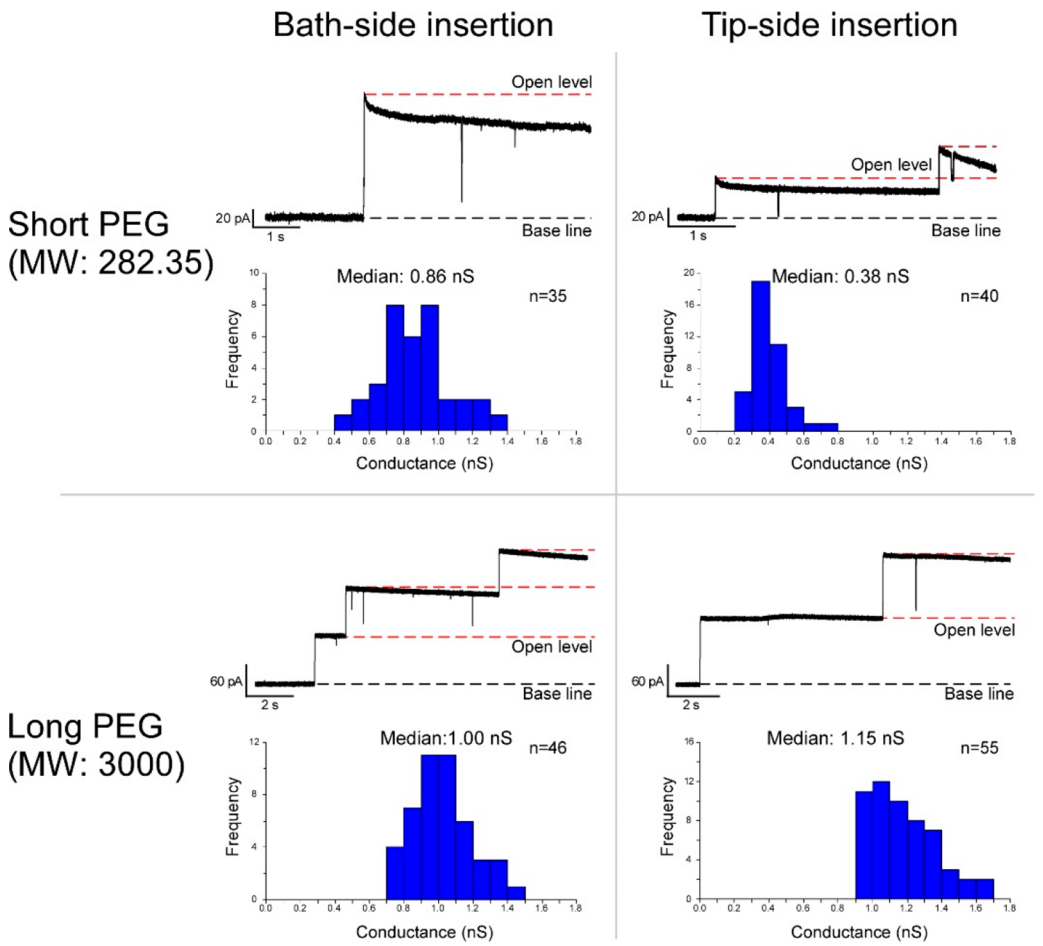

Figure 2. Measured conductance through the *α*HL pore is affected by (top and bottom) the length of the supporting PEG monolayer and (left and right) insertion side. For example, median conductance values when using a short PEG (282.35 g/mol) at an applied potential of 100 mV were 0.86 and 0.38 nS using bath-side and tip-side insertion methods, respectively. In contrast, the values were 1.00 and 1.15 nS (bath side and tip side) when a longer PEG layer (3000 g/mol) was employed. The observation of multiple step increases in channel current is consistent with additional protein insertions (acting as resistors in parallel).

vibrational and high voltage (≳250 mV) perturbations. As such, numerous developments of methods for the formation of lipid bilayer membranes have been reported for channel measurements. For example, a droplet contact method[23−25] and droplet interface bilayers[26,27] that form bilayer membranes by contacting droplets that are surrounded by a lipid

DOI: 10.1021/acsnano.8b09667
ACS Nano XXXX, XXX, XXX−XXX

monolayer have been reported as a simple and easy method to prepare stable lipid bilayer membranes. Glass micro- and nanopore membranes[28−30] also provide a stable platform to support lipid bilayers across small (<20 μm) orifices for protein channel measurements. In recent years, glass pipet supported lipid bilayers serve as ion channel probes[31−35] for the development of imaging probes employed in scanning ion conductance microscopy (SICM). For example, we recently reported the development of single-barrel imaging probes that support a lipid bilayer membrane and reconstituted α-hemolysin (αHL) channels as a means to obtain both chemical and ion concentration profile information using a SICM.[32] Baker and colleagues reported similar strategies employing both single- and double-barrel probes.[33,34]

In an another approach, Ide and co-workers introduced the use of a polyethylene glycol (PEG)-modified, etched gold electrode to support lipid bilayers and thus protein channel measurements.[36,37] In their measurements, ion channel proteins were immobilized on the tip of the gold nanoneedles, and the channel activities of a single ion channel were measured. The advantage of this approach is that the bilayer is formed by pushing two lipid monolayer leaflets together, one oriented tail-out on the surface of the PEG-modified electrode and the other at an oil/lipid aqueous interface. As such, the lipid bilayer is not suspended across a pore orifice, rather it separates a small volume aqueous reservoir between the lipid bilayer and gold electrode (tip side) and a bath reservoir on the opposite side of the membrane. The bilayer formation is relatively facile compared to the methods described above and requires only that the gold electrode be immersed across this oil/lipid aqueous interface.

Although Ide and co-workers demonstrated the utility of the PEG-modified gold nanoneedles for lipid bilayer membrane formation and channel measurements, in this article, we quantitatively characterize the performance of the probe, study the effects of probe surface chemistries, and demonstrate control over the direction of freely diffusing protein insertion. We find that the current through the protein channel and at the gold electrode is supported by double-layer charging at the electrode surface. Furthermore, we optimize the PEG length and the salt concentration of electrolyte baths for stable current recordings and apply the probe for spatially resolved chemical detection. The nanoneedle-probe-supported biological nanopore promises to improve the spatial resolution of, for example, bio-SICM probes because of the nanometer scale tip size.

RESULTS AND DISCUSSION

The etched and modified gold nanowire, when immersed across a lipid/oil aqueous interface, supports a lipid bilayer membrane that is able to allow single ion channel measurements (Figures 1 and 2). Similar to previous reports by Ide and co-workers,[35,36] the PEG-layer-modified electrode is able to support a lipid bilayer as verified by the insertion of αHL channels into the lipid bilayer. In this study, we demonstrate that the protein channel can be incorporated from either the tip side (tip-side insertion) or from the bath side (bath-side insertion) as the previous study only demonstrated bath-side reconstitution.[35,36] Tip-side insertion involves incorporating the channel from the aqueous solution within the PEG monolayer between the bottom leaflet of the bilayer membrane and electrode surface (Figure 1). Conversely, bath-side insertion occurs when αHL monomers are present in the bath solution on the opposite side of the membrane from the nanoneedle. In addition to protein insertion orientation, here we demonstrate how the length of the PEG monolayer affects channel conductance and how asymmetric salt concentrations can overcome current drift presumably caused by the capacitive charging of the double layer at the surface of gold nanoneedle electrodes.

Effects of PEG Monolayer Length and Protein Insertion Direction on Channel Measurements. The length of the PEG monolayer used to modify the surface of the gold nanoprobe has noticeable effects on the stability, conductance, and overall performance of the protein channel measurement. Specifically, we investigated the effects of two different thiolated PEGs—a short (MW = 282.35; length = ~1.8 nm) and long (MW = 3000; length = ~24 nm) PEG monolayer by evaluating the pore conductance. The direction of αHL pores should also be considered in order to apply the nanopore-based lipid bilayer platform to chemical detection because the binding and/or translocation of molecules can depend on the direction of the pore. For example, single-stranded DNAs and RNAs more easily translocate from the *cis* side of αHL pores, whereas βCDs do not bind the αHL pores when entering from the *cis* side.[37] Figure 2 shows typical channel currents of αHL pores and histograms of the initial pore conductance with different directions and PEG lengths. The observed channel currents of αHL pores were successfully obtained with insertion of αHL from both directions (tip or bath side) and both PEG lengths tested.

When the αHL nanopores were reconstituted into the lipid bilayer from the bath side, a similar pore conductance was obtained regardless of the PEG length. The median initial pore conductances of αHL with the short and the long PEG-modified nanoneedles are 0.86 ± 0.21 and 1.00 ± 0.17 nS, respectively, in 1 M KNO_3 symmetric salt conditions (Figure 2). Although the initial pore conductance with the short PEG is not much different than that of the long PEG, we observe a decay of the channel current several seconds after pore reconstitution when using the shorter PEG (Figure 2 and Figure S1). We hypothesize that the current decay is caused by the much smaller volume of the tip-side PEG layer when employing the short PEG. The ion concentration in the PEG layer after the channel current measurements can be estimated by the volume of the PEG layer and the charge flux. The volume of the PEG layer can be calculated from the geometry of the nanoneedle and the PEG length. The shape of the nanoneedle is the combination of a cone and a cylinder with a cone angle of 20° and the cylinder diameter of 250 μm (Figure S2). The total height of the nanoneedle is defined as the height of the lipid/oil mixture in the bath chamber and is ~2 mm. As a result, the surface area of the nanoneedle can be calculated as 1.30 mm^2, and the volumes of the PEG layer with the short (1.8 nm) and the long (24 nm) PEG are 2.4 and 31.2 pL, respectively. The charge flux during the first 30 s and the initial number of ions in the PEG layer with the long PEG-modified nanoneedles are 66.9 pC/s and 1.88×10^{13}, respectively. As a result, the concentration change in ion composition in the PEG layer during the first 30 s is ~2.1%. Because the volume with the short PEG is about 13 times smaller (2.4 pL), the concentration change of ions in the tip-side volume of the PEG-modified nanoneedle would be more than 10 times larger than that of the long PEG-modified nanoneedle, leading to a more rapid current decay.

DOI: 10.1021/acsnano.8b09667
ACS Nano XXXX, XXX, XXX−XXX

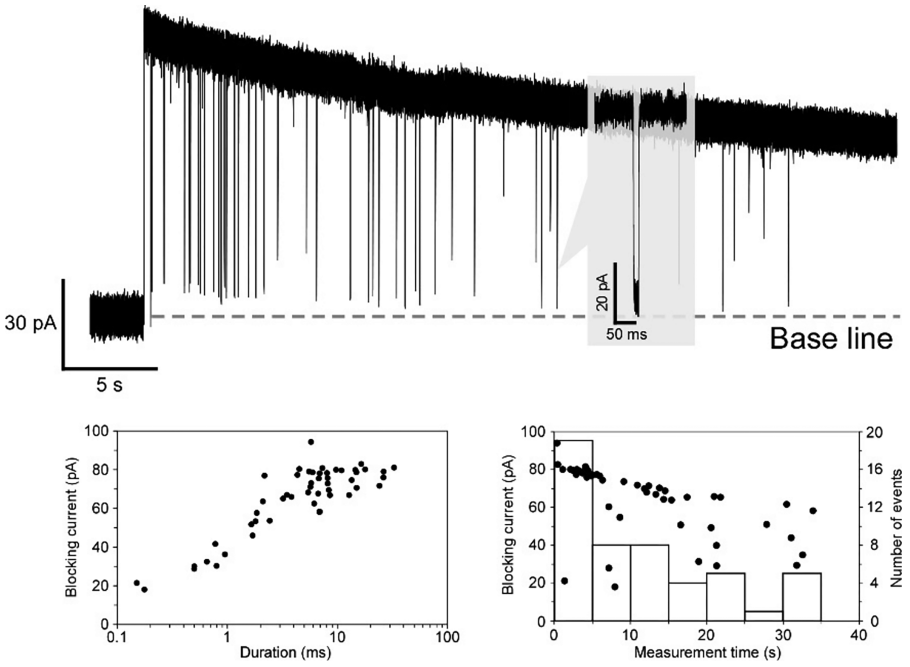

Figure 3. Tip-side insertion method allows the detection of bath-side βCD. (Top) Single-βCD events are indicated by resistive pulses at ~85% of the open channel current. (Bottom left) βCD binding events block, on average 82% of the open channel current, with a mean dwell time of 7.8 ms. However, over the course of the experiment, (bottom right) the blocking current and number of events decreased. In addition, we observed a reproducible decay in the open channel current discussed below.

Protein conductance using tip-side insertion exhibited a much stronger dependence on PEG length. With the tip-side insertion of αHL, the median initial pore conductance of αHL is 0.38 ± 0.10 and 1.15 ± 0.19 nS for short and long PEG, respectively (Figure 2). The pore conductance with the short PEG is much lower than what is observed with the longer PEG.

We hypothesize that the pore conductance relates to the extent of physical blocking of the protein pore aperture, which changes with the direction of insertion and the length of PEG. This is because the distance between the pore opening and the surface of the nanoneedle changes with PEG length and the direction of the nanopore. The long PEG layer, ~24 nm in length, is much longer than the *cis* portion of the protein, thus there is space for ions to move freely to and from the aperture of hemolysin. On the other hand, the short PEG length is only ~1.8 nm which, regardless of protein orientation, creates an impediment to ion flow through the protein channel, leading to a lower overall observed conductance value. This effect is exacerbated when using tip-side insertion of αHL nanopores, which led to conductance values that were much lower than those of the bath-side-inserted αHL because the length of the short PEG (~1.8 nm) is smaller than the extramembrane portion of αHL (~6 nm).[38] We also measured the channel current of SLO nanopores with the long PEG-modified nanoneedle (Figure S3). Although these channels are much larger (>10 nm) in comparison to αHL nanopores, we successfully measured channel currents. From this result, the long PEG-modified nanoneedle allows us to utilize other kinds of biological nanopores that have larger pore diameter.

S_7βCD Detection Using the Nanoneedle-Based Nanopore Probe. To demonstrate the resistive-pulse chemical detection abilities of the nanoneedle-based probe, similar to a traditional bilayer cup setup,[37,39,40] we detected binding events of S_7βCD molecules with αHL pores. Figure 3 shows the typical current−time trace indicating single blockade events as S_7βCD enters an αHL pore. The scatter plots of blocking current magnitude and duration caused by S_7βCD binding events are also shown in Figure 3. S_7βCD binding events were clearly observed using the long PEG-modified nanoneedle-based biological nanopore probe with the tip-side insertion of αHL nanopores (the correct orientation for S_7βCD binding events).

Effects of Electrode Double-Layer Charging on Observed Current−Time Traces. The open channel current, in symmetrical 1.0 M KNO_3 solutions, is not stable over several seconds. More specifically, we observe a reproducible drift in the open channel current over the time scale of seconds to minutes (Figure 3). In addition, the frequency of S_7βCD binding events dramatically decreased after several seconds of recording (Figure 3). We hypothesize that the decay of the open channel current is caused by charging up the electric double layer of the surface of the gold nanoneedle (which likely carries the current at the gold electrode). The decrease of S_7βCD binding events also relates to the double-layer charging. As the potential drop decreases across the nanopore by charging up the electric double layer, the electrophoretic force acting on the S_7βCD molecules drops and the frequency of S_7βCD binding events also decays.[41] To better understand the observed current decay, the gold nanoneedle-based biological nanopore probe can be described as an equivalent circuit in which the capacitance of the electric double layer and the resistance of the αHL nanopore are connected in series (Figure S4). The time-dependent current $i(t)$ response should follow eq 1.

$$i(t) = \frac{V}{R} e^{-t/R_p C_d} \quad (1)$$

In eq 1, V is the applied potential between the gold nanoneedle and the reference electrode, and R_p and C_d indicate

DOI: 10.1021/acsnano.8b09667
ACS Nano XXXX, XXX, XXX−XXX

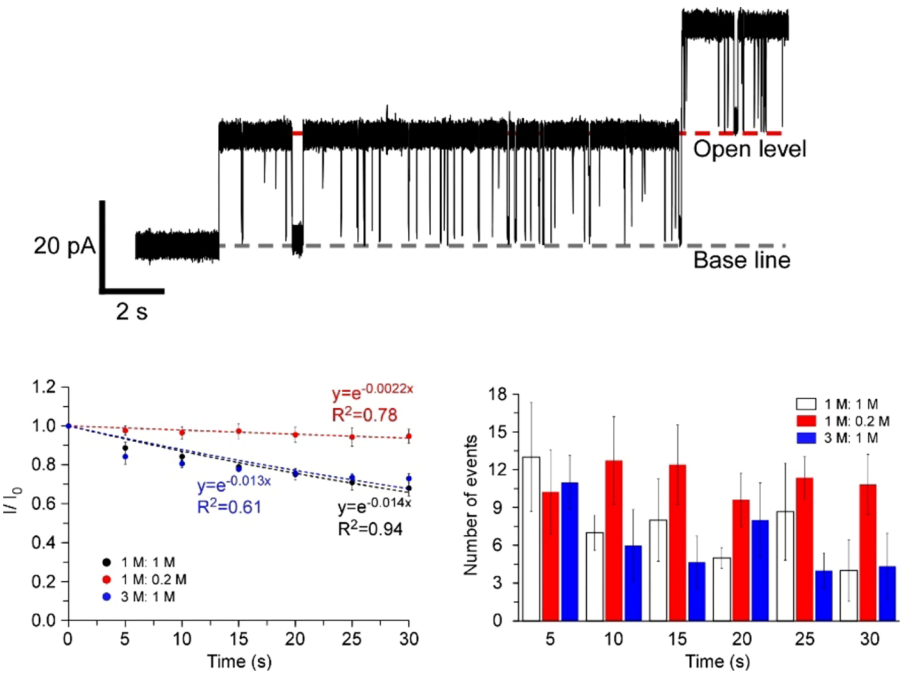

Figure 4. Introduction of asymmetric salt concentrations (tip side/bath side) circumvents the decay in open channel current. (Top) Typical current−time traces of αHL nanopores with βCD in the asymmetric salt condition (tip side/bath side = 1 M/0.2 M) exhibits a much more stable open channel current while still allowing for single-molecule measurements. (Bottom left) Rate of open channel current decay (I/I_0) is a function of the asymmetric salt conditions. In addition (bottom right), the binding event frequency is affected by the current decay and salt conditions. At a tip side/bath side ratio of 1 M/0.2 M, the βCD binding event frequency remains constant during the time frame of an experiment where, at ratios of 1:1 M and 3:1 M, event frequency decreases throughout the experimental time scale.

the resistance of the nanopore and the capacitance of the double layer, respectively. The applied potential is +100 mV, and the pore resistance when the αHL is reconstituted from the tip side and the lipid bilayer was formed by the long PEG-modified gold nanoneedle is 0.87 GΩ. The capacitance of the gold nanoneedle is calculated by the capacitance per unit area of the double layer of the gold surface and the surface area of the gold nanoneedle immersed in the lipid/oil mixture. The capacitance per unit area of the double layer of the PEG-modified gold surface is expected to be ∼5 μF/cm^2.[42] Because the shape of the nanoneedle tip is a combination of a circular cone and cylinder, the surface area is calculated as $\pi r_n m + 2r_w \pi h$, where r_n is the radius of the nanoneedle, m is the length of the conical generatrix, r_w is the radius of the gold wire, and h is the length of the cylinder. The estimated surface area is 1.3 mm^2. The calculated time-dependent circuit current should decay to ∼60% of the initial value in 30 s. This time response is similar to the recorded current decay experimentally (Figure S4). Furthermore, the potential across the nanopore is calculated as $i(t) \times R_p$, and the potential also decays to ∼60% of the initial value in 30 s. As a result, the electrophoretic force acting on the S$_7$$\beta$CD molecules that is dependent on the electric field would be reduced and the event frequency also decayed.

Improvement of Decays of Channel Current and Event Frequency. To improve the observed decay in channel current and event frequency, we applied asymmetric salt conditions to the tip and bath solutions. The typical recorded channel currents with asymmetric salt conditions of 3 M/1 M and 1 M/0.2 M KNO_3 (tip/bath solution) are shown in Figure S5 and Figure 4. Normalized channel currents and numbers of S$_7$$\beta$CD binding events every 5 s with salt conditions of 1 M/1 M, 3 M/1 M, and 1 M/0.2 M KNO_3 (tip/bath solution) are shown in Figure 4. With the salt condition of 3 M/1 M and 1 M/1 M KNO_3, the channel currents decreased more than 10% over 5 s. Each then decayed to ∼70% of the initial value over ∼30 s. The event frequencies of S$_7$$\beta$CD binding also dropped to half the initial frequencies (*i.e.*, in first 5 s), gradually decreasing afterward. With the salt condition of 1 M/0.2 M KNO_3, on the other hand, the channel current was almost maintained at the initial value, and the decay within the first 30 s was less than 5%. In addition, S$_7$$\beta$CD binding event frequency was maintained at around the initial event frequency (2.20 ± 0.27/s). As the decay of the channel current and the event frequency are hypothesized to be caused by double-layer charging at the electrode interface, a higher pore resistance can decrease the RC time constant. The pore resistances of the αHL nanopore with asymmetric salt conditions of 3 M/1 M and 1 M/0.2 M KNO_3 that are calculated from the initial open-level channel current was 0.8 and 4.0 GΩ, respectively. The decay rate of the calculated open channel current with 4.0 GΩ pore resistance is very close to one of the measured currents with the asymmetric salt condition of 1 M/0.2 M KNO_3 (Figure S4). As a result, the decays of the channel current and event frequency were extended with the salt condition of 1 M/0.2 M KNO_3, due to the higher pore resistance. As a future plan, the use of the equilibrium electrodes such as the Ag/AgCl electrode as the nanoneedles would improve the current decay caused by double-layer charging without the need to use asymmetric salt conditions.

The frequency of S$_7$$\beta$CD binding events is a function of the concentration of S$_7$$\beta$CD (Figure 5). We recorded current−time traces in bath solutions of S$_7$$\beta$CD at concentrations of 10, 50, 100, and 200 μM using the long PEG-modified nanoneedle probe and asymmetric salt condition of 1 M/0.2 M KNO_3 (tip/bath solution). The event frequencies with the S$_7$$\beta$CD

DOI: 10.1021/acsnano.8b09667
ACS Nano XXXX, XXX, XXX−XXX

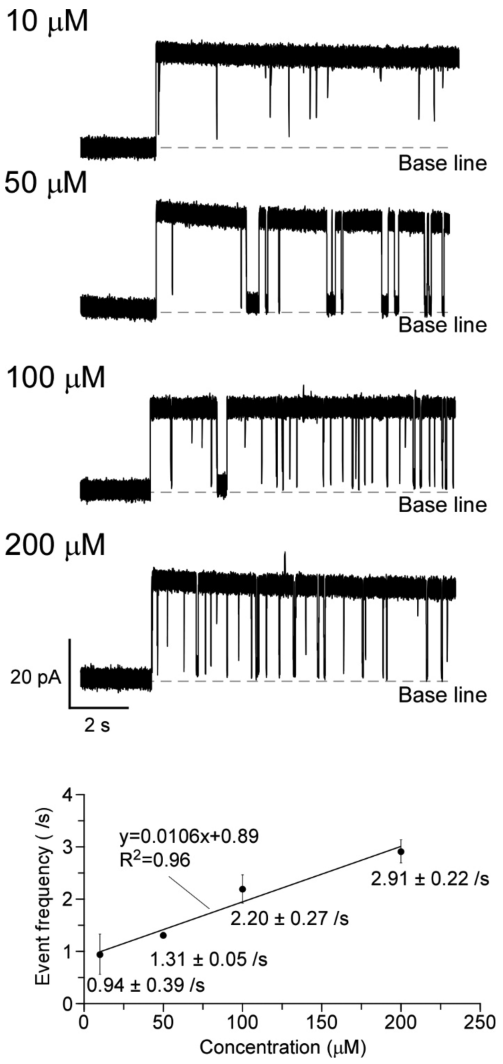

Figure 5. Frequency of βCD binding events is a function of the concentration of βCD in the bath-side solution. The graph shows the calibration curve of the βCD concentration and the event frequency. More specifically, the event frequency is linearly related to the concentration of βCD (n > 3).

concentration of 10, 50, 100, and 200 μM in the initial 30 s after the single pore reconstitution are 0.94 ± 0.39 (n = 4), 1.31 ± 0.05 (n = 3), 2.20 ± 0.27 (n = 5), and 2.91 ± 0.22/s (n = 4), respectively (Figure 5 and Table S1). The number of blocking signals caused by the $S_7\beta$CD binding clearly increased with increasing $S_7\beta$CD concentration. The event frequency *versus* the $S_7\beta$CD concentration relationship was linearly fitted with a high correlation factor (R^2) (mean R^2 value of 0.96, n = 3) in the range from 10 to 200 μM $S_7\beta$CD concentration (Figure 5), and the intercept of the calibration curve does not pass through the origin. Previously, we reported the detection of βCD binding events with an αHL nanopore. The nature of the calibration curve is a function of the concentration window employed. For example, when using a low concentration window (10−50 μM), the calibration curve passes through the origin. At high concentration regions (0.5−5 mM), the binding event frequency is underestimated on account of not being able to distinguish closely spaced events, and as such, the calibration curve does not pass through the origin.[40] In the present study, as we measured βCD binding events at a relatively high concentration, the calibration curve did not pass through the origin.

Determination of $S_7\beta$CD Concentration in the Microchannel with a Nanoneedle-Based Nanopore Probe. The nanoneedle probe enables spatially resolved concentration profile measurements, demonstrated using a microfluidic channel device to generate a linear concentration gradient profile. The microchannel comprised two main parallel channels and a narrow perpendicular channel connecting the two main channels. The concentration gradient of $S_7\beta$CD is generated in the narrow channel by flowing the solutions with higher and lower $S_7\beta$CD from each inlet of the main channels. The simulated concentration mapping in the microchannel and graph of $S_7\beta$CD concentration in the narrow channel are shown in Figure 6. The $S_7\beta$CD concentration in the narrow channel changes linearly between the two main channels, and the $S_7\beta$CD concentrations at open spaces (x = 5.75, 11.75, and 17.75 mm) are 150, 100, and 50 μM, respectively. The frequencies of the $S_7\beta$CD binding events also estimated at 2.48, 1.95, and 1.42/s using the calibration curve.

The typical recorded channel currents and the plots of the event frequency of $S_7\beta$CD binding events at each open space (x = 5.75, 11.75, and 17.75 mm) are shown in Figure 6. $S_7\beta$CD binding events were obtained at each open space, and the event frequency was clearly different at each open space. The event frequencies at each open space (x = 5.75, 11.75, and 17.75 mm) were 2.94 ± 0.33, 1.96 ± 0.09, and 1.18 ± 0.48/s (n > 3), respectively. From these results, the concentrations at each open space were calculated as 192, 101, and 27 μM. Although the gradient of the fit curve was larger than the simulated value, the measured $S_7\beta$CD concentrations followed a linear trend (Figure 6). The larger gradient indicates that the concentration distribution in the narrow channel did not reach static state (Figure S6).

CONCLUSION

In conclusion, we improved the operational parameters of the nanoneedle-based ion channel recording method that Ide and co-workers previously reported and applied it as the local nanopore sensing method by combining with microfluidic technologies. First, we optimized the length of the modified PEG to obtain a suitable conductance of αHL nanopores and controlled the direction of αHL insertion to allow detection of target chemicals. As a result, the gold nanoneedle modified with the long PEG provided the expected pore conductance of αHL for both directions of the αHL pore. We also demonstrated detection of binding events of $S_7\beta$CD molecules in αHL pores with the biological nanopore probe when αHL proteins were inserted from the tip side. Although the binding events were detected, the channel current of the open level and the event frequency of $S_7\beta$CD binding decayed in a few seconds. To prolong these decays, we applied the asymmetric salt condition of 1 M/0.2 M KNO_3 to the solutions of the tip and the bath sides. As a result, the event frequency and the channel current were maintained at initial values more than 30 s, and the event frequency was 2.20 ± 0.27/s with the $S_7\beta$CD concentration of 100 μM and the applied potential of 100 mV. The event frequency was linearly changed between the concentration range of 10 to 200 μM. Finally, we demonstrated the ability to achieve spatially resolved measurements by measuring the $S_7\beta$CD concentration in a concentration gradient, generated in the microchannel, with the nanopore probe. We believe that our nanoneedle-based

DOI: 10.1021/acsnano.8b09667
ACS Nano XXXX, XXX, XXX−XXX

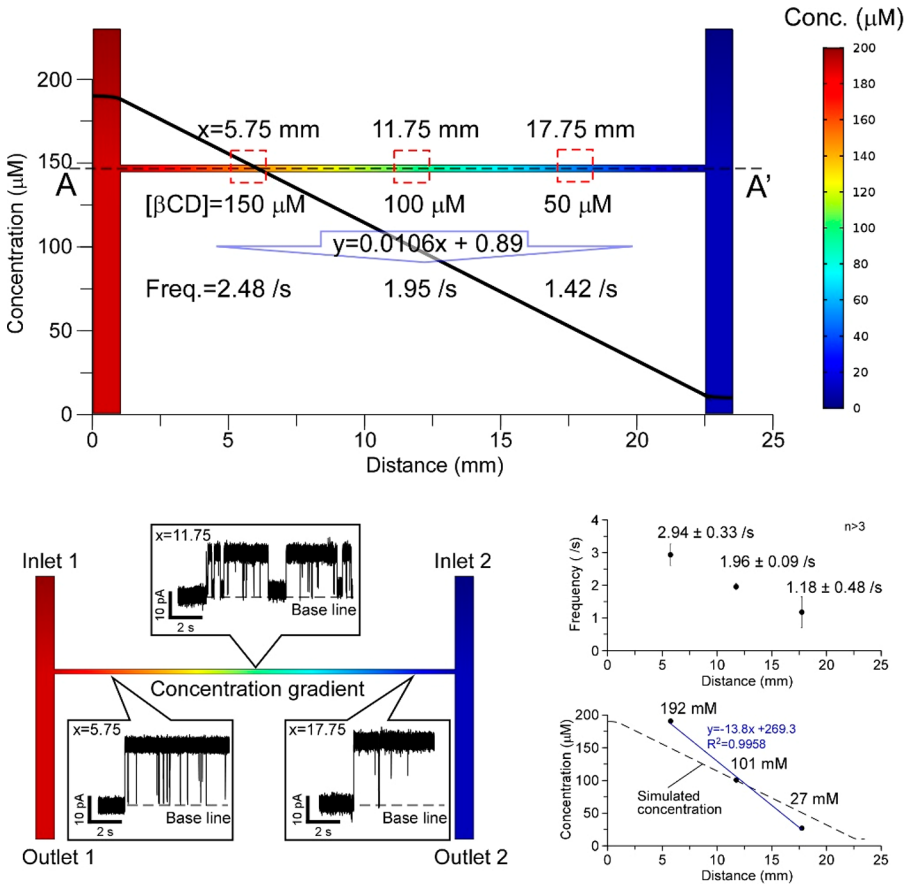

Figure 6. Nanoneedle-based nanopore probe enables spatially resolved measurements. The concentration gradient of βCD was generated by flowing the solution with and without βCD to the H-shaped microchannel, and the βCD concentration was measured with the nanoneedle-based nanopore probe. (Top) βCD concentration was simulated by the hydrodynamic simulation. The concentration gradient of βCD was linearly generated in the narrow channel, and the frequency of the βCD binding events was calculated from the calibration curve. (Bottom left) Typical current−time traces of αHL nanopores at each point. (Bottom right) Event frequency decreased with increasing the *x* distance, and the measured βCD concentration shows the linear gradient.

nanopore sensor platform has a potential to allow much higher spatial resolution as a scanning probe for use in bio-SICM.

EXPERIMENTAL METHODS

Reagents and Chemicals. Calcium chloride ($CaCl_2$; Sigma-Aldrich) was used for electrochemical etching to fabricate a gold nanoneedle. A 250 μm diameter gold wire of 99.95% purity (Alfa Aesar) was used as a material of the gold nanoneedle. Thiol-dPEG4-acid (MW 282.35; Quanta BioDesign) and *O*-(3-carboxypropyl)-*O*′-[2-(3-mercaptopropionylamino)ethyl]propylethylene glycol (MW 3000; Sigma-Aldrich) were used as short and long thiolated polyethylene glycol (thiol-PEG), respectively. 1,2-Diphytanoyl-*sn*-glycero-3-phosphocholine (DPhPC; Avanti Polar Lipid), cholesterol from ovine wool (Chol; Avanti Polar Lipid), and *n*-decane (Merck Millipore Corp.) were used as the lipid/oil solution. Potassium nitrate (KNO_3; Sigma-Aldrich) and sodium phosphate buffer (pH 7.4) made with sodium dihydrogen phosphate ($NaH_2PO_4{\cdot}2H_2O$; Sigma-Aldrich) and sodium hydrogen phosphate ($Na_2HPO_4{\cdot}2H_2O$; Sigma-Aldrich) were used as the aqueous electrolyte solution. The buffer solution was prepared using ultrapure water from a Milli-Q (Merck Millipore Corp.) resist of 18.2 MΩ at 25 °C. α-Hemolysin (αHL; Sigma-Aldrich) isolated from *Staphylococcus aureus* and Streptolysin O (SLO; Sigma-Aldrich) isolated from *Streptococcus pyogenes* were obtained as a monomer protein in the form of a powder. For use, samples were diluted to the designated concentration using a buffered electrolyte solution and stored at 4 °C. Heptakis(6-*O*-sulfo)-β-cyclodextrin heptasodium salt (S_7βCD; Sigma-Aldrich) was used as the chemical for nanopore sensing. DL-Dithiothreitol (DTT; Sigma-Aldrich) was used as the reducing agent for SLO nanopores.

Preparation of a PEG-Modified Gold Nanoneedle. A gold nanoneedle (Figure S2) was fabricated by electrochemical etching of the gold wire in a 2.0 M $CaCl_2$ solution (distilled water). A carbon rod with 3 mm diameter was used as a counter electrode, and a function generator (GFG-8219A; GW Insteck) was used to control the input voltage magnitude and frequency. The 1 mm tip of the gold wire was vertically immersed in the $CaCl_2$ solution. Then, a sine wave AC voltage was applied between the gold wire and the counter electrode until the current reached zero, typically in 60 min. The typical conditions of the applied voltage were AC voltage of 12 $V_{peak\ to\ peak\ (p\text{-}p)}$ at 1 kHz with a DC offset of 9.5 V.

The nanoneedle was modified with thiol-PEG to prepare a hydrophilic surface sufficient to support a lipid bilayer membrane. First, the gold nanoneedle was electrochemically cleaned to prepare a fine gold surface. See Supporting Information for details of the cleaning method of the gold nanoneedle. Then, the tip of the gold nanoneedle was immersed in 60 mg/mL thiol-PEG solution (in ethanol) for 2 h at room temperature. Finally, the nanoneedle was rinsed with ethanol and deionized water.

Formation of a Lipid Bilayer Membrane. A bath solution of two immiscible layers that are aqueous electrolyte solutions (1 M KNO_3, 20 mM sodium phosphate buffer, pH 7.4) and the oil/lipid mixture (20 mg/mL DPhPC for αHL nanopores or DPhPC/cholesterol = 7:3 (mol/mol) for SLO nanopores in *n*-decane) was prepared. The layered solution consisting of the oil/lipid mixture in the top layer and the aqueous electrolyte solution in the bottom layer

DOI: 10.1021/acsnano.8b09667
ACS Nano XXXX, XXX, XXX−XXX

is formed, and a lipid monolayer is formed at the interface between these two layers. The PEG-modified gold nanoneedle was dipped in the electrolyte solution for 10 min and then immersed in the bath solution. The tip-side aqueous solution is drawn from the solution into which the tip is dipped prior to being inserted into the bath. A lipid bilayer membrane is formed on the tip when the tip is pushed through the interface of these two layers. The movement distance was manipulated with a three-axis manual micromanipulator (Newport Corp.).

Channel Current Measurements of Biological Pores. We applied two lengths of PEG and two insertion directions of αHL pores to the nanoneedle-based lipid bilayer platform and measured channel currents of each pattern. Thiol-PEGs with molecular weight of 282.35 and 3000 g/mol were used as a "short" and "long" length PEG, respectively. The direction of αHL pores was controlled by placing αHL in either aqueous electrolyte solution of bath or tip side. To reconstitute from the tip side, the nanoneedle was dipped in the electrolyte solution (1 M KNO_3, 20 mM sodium phosphate buffer, pH 7.4) containing 30 mM αHL for 10 min before immersing the nanoneedle into the bath solution. From bath side, the aqueous electrolyte solution with 15 mM αHL was used as the bath solution. For the reconstitution of SLO nanopores, SLO was dissolved in the electrolyte solution (0.2 M KNO_3, 10 mM DTT, 20 mM sodium phosphate buffer, pH 7.4) at 32 nM, and it is used as the bath solution. The quasi-reference-counter Ag/AgCl electrode was also immersed in the aqueous electrolyte solution in the bath chamber, and a potential of +100 mV was applied to the tip side. Channel currents were monitored using a patch clamp amplifier (PICO 2, Tecella) with a 7.9 kHz low-pass filter at a sampling frequency of 40 kHz. Analyses of channel signals were performed using pCLAMP version 10.7 (Molecular Devices).

$S_7\beta$CD Detection and Analysis. To demonstrate the chemical detection using the nanoneedle-based nanopore probe, we added $S_7\beta$CD at a concentration of 100 μM to the bath aqueous solution (*trans* side). We used the long PEG-modified nanoneedle-based nanopore probe, and αHL was reconstituted from the tip side. A potential of +100 mV was applied to the tip side (*cis* side), and channel currents were monitored with the patch clamp amplifier. For the analysis of the S7βCD binding events, the channel current data with the single αHL nanopore of the initial 30 s after the pore reconstitution were utilized.

$S_7\beta$CD Detection with Asymmetric Salt Conditions. To extend the decays of the channel current of αHL pores and increase the frequency of $S_7\beta$CD binding events,[43] we applied asymmetric salt conditions in aqueous electrolyte solutions of the tip and bath sides. Salt conditions of 3 M/1 M KNO_3 and 1 M/0.2 M KNO_3 (tip/bath) were applied, and the channel currents at +100 mV were measured. The long PEG-modified nanoneedle-based nanopore probe was used, and αHL was reconstituted from the tip side. The concentration of $S_7\beta$CD in the bath aqueous solution (*trans* side) was 100 μM.

Detection of $S_7\beta$CD Concentration Inside a Concentration Gradient Microchannel. To demonstrate our nanoneedle-based nanopore probe could achieve spatially resolved chemical sensing, we measured $S_7\beta$CD concentration in a concentration gradient microchannel. As the concentration microchannel, an H shape microchannel was prepared (Figure S7). The microchannel is composed of two main channels, and a narrow channel connects two main channels. The widths of the main and the narrow channels are 1.0 and 0.25 mm, respectively, and the depth is 0.8 mm. The concentration gradient is generated in the narrow channel by flowing the solutions with different chemical concentration to each main channel.

First, the concentration distribution of $S_7\beta$CD in the microchannel by flowing solutions with 0 and 200 μM $S_7\beta$CD to the inlets 1 and 2 was simulated with COMSOL Multiphysics 5.2a (COMSOL Inc.) using the microfluidic module. The density and viscosity of the solution and the diffusion coefficient were set to 1.0 g/mL, 1.0 mPa·s, and 1.0×10^{-9} m^2/s, respectively. The flow rate was set to 100 μL/h for each inlet. The microchannel was fabricated by cutting acrylic sheets with a laser cutter (VLS3.50, Universal Laser Systems, Inc.) and bonding with an acrylic cement (Weld-on). In order to insert the nanoneedle probe into the narrow channel by the micromanipulator, open spaces (1 mm square) on the narrow channel were constructed. Each solution (0.2 M KNO_3, 20 mM sodium phosphate buffer, pH 7.4) with and without $S_7\beta$CD was flowed to the channel, which is filled by 100 μM $S_7\beta$CD solution (0.2 M KNO_3, 20 mM sodium phosphate buffer, pH 7.4) at 100 μL/h by injecting and sucking with a syringe pump (YSP-202, YSP Co., Ltd.). After 15 min from flowing the solutions, the oil/lipid mixture (20 mg/mL DPhPC in *n*-decane) was added to the open spaces, and the nanoneedle-based nanopore probe in which the long PEG was modified and αHL was reconstituted from the tip side was inserted to the narrow channel passing through the oil/lipid solution. A potential of +100 mV was applied to the tip side, and channel currents were monitored with the patch clamp amplifier.

ASSOCIATED CONTENT

Supporting Information

The Supporting Information is available free of charge on the ACS Publications website at DOI: 10.1021/acsnano.8b09667.

Cleaning procedures of the gold nanoneedle, SEM images of gold nanoneedles, design and photograph of the microchannel, comparison of current decays between the long and short PEG, equivalent circuit of the nanoneedle-based nanopore probe and the calculated decay rates, and typical current−time traces of αHL nanopore with the asymmetric salt condition of 3 M/1 M (PDF)

AUTHOR INFORMATION

Corresponding Author

*E-mail ryan.white@uc.edu.

ORCID

Ryuji Kawano: 0000-0001-6523-0649

Ryan J. White: 0000-0003-0849-0457

Notes

The authors declare no competing financial interest.

ACKNOWLEDGMENTS

This material is based upon work supported by the National Science Foundation under CHE 1608674 and Japan Society for the Promotion of Science (JSPS) research Fellow, and KAKENHI (Grant No. 17K19138) from the MEXT Japan. We thank Dr. Henry S. White and Dr. Martin Edwards for helpful discussions on the current decay.

REFERENCES

(1) Bayley, H.; Braha, O.; Gu, L.-Q. Stochastic Sensing with Protein Pores. *Adv. Mater.* **2000**, *12*, 139−142.

(2) Bayley, H.; Martin, C. R. Resistive-Pulse Sensing From Microbes to Molecules. *Chem. Rev.* **2000**, *100*, 2575−2594.

(3) Bayley, H.; Cremer, P. S. Stochastic Sensors Inspired by Biology. *Nature* **2001**, *413*, 226−230.

(4) Branton, D.; Deamer, D. W.; Marziali, A.; Bayley, H.; Benner, S. A.; Butler, T.; Di Ventra, M.; Garaj, S.; Hibbs, A.; Huang, X.; Jovanovich, S. B.; Krstic, P. S.; Lindsay, S.; Ling, X. S.; Mastrangelo, C. H.; Meller, A.; Oliver, J. S.; Pershin, Y. V.; Ramsey, J. M.; Riehn, R.; et al. The Potential and Challenges of Nanopore Sequencing. *Nat. Biotechnol.* **2008**, *26*, 1146−1153.

(5) Howorka, S.; Siwy, Z. Nanopore Analytics: Sensing of Single Molecules. *Chem. Soc. Rev.* **2009**, *38*, 2360−2384.

(6) Shi, W.; Friedman, A. K.; Baker, L. A. Nanopore Sensing. *Anal. Chem.* **2017**, *89*, 157−188.

DOI: 10.1021/acsnano.8b09667
ACS Nano XXXX, XXX, XXX−XXX

(7) Clarke, J.; Wu, H.-C.; Jayasinghe, L.; Patel, A.; Reid, S.; Bayley, H. Continuous Base Identification for Single-Molecule Nanopore DNA Sequencing. *Nat. Nanotechnol.* **2009**, *4*, 265−270.
(8) Derrington, I. M.; Butler, T. Z.; Collins, M. D.; Manrao, E.; Pavlenok, M.; Niederweis, M.; Gundlach, J. H. Nanopore DNA Sequencing with MspA. *Proc. Natl. Acad. Sci. U. S. A.* **2010**, *107*, 16060−16065.
(9) Venkatesan, B. M.; Bashir, R. Nanopore Sensors for Nucleic Acid Analysis. *Nat. Nanotechnol.* **2011**, *6*, 615−624.
(10) Akeson, M.; Branton, D.; Kasianowicz, J. J.; Brandin, E.; Deamer, D. W. Microsecond Time-Scale Discrimination Among Polycytidylic Acid, Polyadenylic Acid, and Polyuridylic Acid as Homopolymers or as Segments Within Single RNA Molecules. *Biophys. J.* **1999**, *77*, 3227−3233.
(11) Wang, Y.; Zheng, D.; Tan, Q.; Wang, M. X.; Gu, L.-Q. Nanopore-Based Detection of Circulating MicroRNAs in Lung Cancer Patients. *Nat. Nanotechnol.* **2011**, *6*, 668−674.
(12) Zhang, X.; Wang, Y.; Fricke, B. L.; Gu, L.-Q. Programming Nanopore Ion Flow for Encoded Multiplex MicroRNA Detection. *ACS Nano* **2014**, *8*, 3444−3450.
(13) Hiratani, M.; Ohara, M.; Kawano, R. Amplification and Quantification of an Antisense Oligonucleotide from Target MicroRNA Using Programmable DNA and a Biological Nanopore. *Anal. Chem.* **2017**, *89*, 2312−2317.
(14) Fologea, D.; Ledden, B.; McNabb, D. S.; Li, J. Electrical Characterization of Protein Molecules by a Solid-State Nanopore. *Appl. Phys. Lett.* **2007**, *91*, 053901.
(15) Talaga, D. S.; Li, J. Single-Molecule Protein Unfolding in Solid State Nanopores. *J. Am. Chem. Soc.* **2009**, *131*, 9287−9297.
(16) Kowalczyk, S. W.; Hall, A. R.; Dekker, C. Detection of Local Protein Structures along DNA Using Solid-State Nanopores. *Nano Lett.* **2010**, *10*, 324−328.
(17) Watanabe, H.; Gubbiotti, A.; Chinappi, M.; Takai, N.; Tanaka, K.; Tsumoto, K.; Kawano, R. Analysis of Pore Formation and Protein Translocation Using Large Biological Nanopores. *Anal. Chem.* **2017**, *89*, 11269−11277.
(18) Dekker, C. Solid-State Nanopores. *Nat. Nanotechnol.* **2007**, *2*, 209−215.
(19) Miles, B.-N.; Ivanov, A.-P.; Wilson, K.-A.; Doğan, F.; Japrung, D.; Edel, J.-B. Single Molecule Sensing with Solid-State Nanopores: Novel Materials, Methods, and Applications. *Chem. Soc. Rev.* **2013**, *42*, 15−28.
(20) Ma, L.; Cockroft, S. L. Biological Nanopores for Single-Molecule Biophysics. *ChemBioChem* **2010**, *11*, 25−34.
(21) Mueller, P.; Rudin, D. O.; Ti Tien, H.; Wescott, W. C. Reconstitution of Cell Membrane Structure *in Vitro* and Its Transformation into an Excitable System. *Nature* **1962**, *194*, 979−980.
(22) Montal, M.; Mueller, P. Formation of Bimolecular Membranes from Lipid Monolayers and a Study of Their Electrical Properties. *Proc. Natl. Acad. Sci. U. S. A.* **1972**, *69*, 3561−3566.
(23) Funakoshi, K.; Suzuki, H.; Takeuchi, S. Lipid Bilayer Formation by Contacting Monolayers in a Microfluidic Device for Membrane Protein Analysis. *Anal. Chem.* **2006**, *78*, 8169−8174.
(24) Kawano, R.; Tsuji, Y.; Sato, K.; Osaki, T.; Kamiya, K.; Hirano, M.; Ide, T.; Miki, N.; Takeuchi, S. Automated Parallel Recordings of Topologically Identified Single Ion Channels. *Sci. Rep.* **2013**, *3*, 1995.
(25) Shoji, K.; Kawano, R. Microfluidic Formation of Double-Stacked Planar Bilayer Lipid Membranes by Controlling the Water-Oil Interface. *Micromachines* **2018**, *9*, 253.
(26) Hwang, W. L.; Holden, M. A.; White, S.; Bayley, H. Electrical Behavior of Droplet Interface Bilayer Networks: Experimental Analysis and Modeling. *J. Am. Chem. Soc.* **2007**, *129*, 11854−11864.
(27) Bayley, H.; Cronin, B.; Heron, A.; Holden, M. A.; Hwang, W. L.; Syeda, R.; Thompson, J.; Wallace, M. Droplet Interface Bilayers. *Mol. BioSyst.* **2008**, *4*, 1191−1208.
(28) Coronado, R.; Latorre, R. Phospholipid Bilayers Made from Monolayers on Patch-Clamp Pipettes. *Biophys. J.* **1983**, *43*, 231−236.
(29) White, R. J.; Ervin, E. N.; Yang, T.; Chen, X.; Daniel, S.; Cremer, P. S.; White, H. S. Single Ion-Channel Recordings Using Glass Nanopore Membranes. *J. Am. Chem. Soc.* **2007**, *129*, 11766−11775.
(30) Heitz, B. A.; Xu, J.; Hall, H. K.; Aspinwall, C. A.; Saavedra, S. S. Enhanced Long-Term Stability for Single Ion Channel Recordings Using Suspended Poly(Lipid) Bilayers. *J. Am. Chem. Soc.* **2009**, *131*, 6662−6663.
(31) Zhou, Y.; Bright, L. K.; Shi, W.; Aspinwall, C. A.; Baker, L. A. Ion Channel Probes for Scanning Ion Conductance Microscopy. *Langmuir* **2014**, *30*, 15351−15355.
(32) Macazo, F. C.; White, R. J. Bioinspired Protein Channel-Based Scanning Ion Conductance Microscopy (Bio-SICM) for Simultaneous Conductance and Specific Molecular Imaging. *J. Am. Chem. Soc.* **2016**, *138*, 2793−2801.
(33) Shi, W.; Zeng, Y.; Zhou, L.; Xiao, Y.; Cummins, T. R.; Baker, L. A. Membrane Patches as Ion Channel Probes for Scanning Ion Conductance Microscopy. *Faraday Discuss.* **2016**, *193*, 81−97.
(34) Shi, W.; Zeng, Y.; Zhu, C.; Xiao, Y.; Cummins, T. R.; Hou, J.; Baker, L. A. Characterization of Membrane Patch-Ion Channel Probes for Scanning Ion Conductance Microscopy. *Small* **2018**, *14*, 1702945.
(35) Okuno, D.; Hirano, M.; Yokota, H.; Onishi, Y.; Ichinose, J.; Ide, T. A Simple Method for Ion Channel Recordings Using Fine Gold Electrode. *Anal. Sci.* **2016**, *32*, 1353−1357.
(36) Okuno, D.; Hirano, M.; Yokota, H.; Ichinose, J.; Kira, T.; Hijiya, T.; Uozumi, C.; Yamakami, M.; Ide, T. A Gold Nano-Electrode for Single Ion Channel Recordings. *Nanoscale* **2018**, *10*, 4036−4040.
(37) Gu, L.-Q.; Braha, O.; Conlan, S.; Cheley, S.; Bayley, H. Stochastic Sensing of Organic Analytes by a Pore-Forming Protein Containing a Molecular Adapter. *Nature* **1999**, *398*, 686−690.
(38) Song, L.; Hobaugh, M. R.; Shustak, C.; Cheley, S.; Bayley, H.; Gouaux, J. E. Structure of Staphylococcal α-Hemolysin, a Heptameric Transmembrane Pore. *Science* **1996**, *274*, 1859−1865.
(39) Gu, L.-Q.; Dalla Serra, M.; Vincent, J. B.; Vigh, G.; Cheley, S.; Braha, O.; Bayley, H. Reversal of Charge Selectivity in Transmembrane Protein Pores by Using Noncovalent Molecular Adapters. *Proc. Natl. Acad. Sci. U. S. A.* **2000**, *97*, 3959−3964.
(40) Lazenby, R. A.; Macazo, F. C.; Wormsbecher, R. F.; White, R. J. Quantitative Framework for Stochastic Nanopore Sensors Using Multiple Channels. *Anal. Chem.* **2018**, *90*, 903−911.
(41) Świetlow, A.; Skoog, M.; Johansson, G. Double-Layer Capacitance Measurements of Self-Assembled Layers on Gold Electrodes. *Electroanalysis* **1992**, *4*, 921−928.
(42) Menz, B.; Knerr, R.; Göpferich, A.; Steinem, C. Impedance and QCM Analysis of the Protein Resistance of Self-Assembled PEGylated Alkanethiol Layers on Gold. *Biomaterials* **2005**, *26*, 4237−4243.
(43) Wanunu, M.; Morrison, W.; Rabin, Y.; Grosberg, A. Y.; Meller, A. Electrostatic Focusing of Unlabelled DNA into Nanoscale Pores Using a Salt Gradient. *Nat. Nanotechnol.* **2010**, *5*, 160−165.

DOI: 10.1021/acsnano.8b09667
ACS Nano XXXX, XXX, XXX−XXX